Geophysical Journal International

Geophys. J. Int. (2023) **232,** 1590–1599
Advance Access publication 2022 October 20
GJI Rock and Mineral Physics, Rheology

https://doi.org/10.1093/gji/ggac409

Mapping faults in the laboratory with seismic scattering 1: the laboratory perspective

Thomas King,[1,2] Luca De Siena,[3,4] Philip Benson[5] and Sergio Vinciguerra[2]

[1]*National Buried Infrastructure Facility, School of Civil Engineering, University of Birmingham, Birmingham B152TT, UK*
[2]*Department of Earth Sciences, University of Turin, Via Tommaso Valperga Caluso,* 35, 10125 *Turin, Italy. E-mail: sergiocarmelo.vinciguerra@unito.it*
[3]*Department of Geophysics, Institute of Geosciences, Johannes Gutenberg University, Mainz,* 55128, *Germany*
[4]*Department of Geology and Petroleum Geology, School of Geosciences, University of Aberdeen, King's College, Aberdeen AB243FX, UK*
[5]*Rock Mechanics Laboratory, School of Earth and Environmental Sciences, University of Portsmouth, Burnaby Building, Portsmouth PO13QL, UK*

Accepted 2022 October 18. Received 2022 October 5; in original form 2021 December 15

SUMMARY

Seismic waves produced by stressed and deforming rocks lose coherence when they cross regions of high heterogeneity. The delay in the arrival of maximum seismic energy amplitude (peak delay), an essential attribute to model earthquake source characteristics, is increasingly used to map complex crustal geology, heterogeneous reservoirs and fault networks. However, no laboratory calibration for the sensitivity of this parameter to fractures is currently available due to both experimental challenges and the difficulty in modelling wavefields in the near field. In this study, peak delays have been measured and mapped in space in the frequency range 50 kHz to 1 MHz using acoustic emission data recorded during a triaxial deformation experiment of Darley Dale Sandstone. Peak delays can increase dramatically throughout the experiment, but their behaviour depends on frequency and, especially, anomalous azimuth-dependent scattering. The changes in frequency depend on strain. At low frequencies, peak delays are sensitive to surface waves generated at the sample boundaries, but they also mark the zones of shadow and intense/intermediate strains expected for an heterogeneous sample. At high frequencies, peak delays detect the zone of intense strain corresponding to the post-deformation shear zone. Temporal variations of peak delays show a frequency-dependent sensitivity to fracture nucleation, fault coalescence and sample failure. Scattering from these heterogeneities produces waves reverberating through seismic coda if the source–station path is close to an acoustic boundary, such as the fault zone or the sample boundaries. Our results confirm that peak delay has notable sensitivity to heterogeneity and can map and monitor structural- and deformation-induced changes in the near-field. The companion modelling paper tests this sensitivity and the corresponding imaging potential.

Key words: Fracture and flow; Acoustic properties; Interface waves; Seismic attenuation; Wave propagation; Wave scattering and diffraction.

1 INTRODUCTION

When seismic waves propagate into the Earth, they suffer energy losses due to scattering and reverberations on Earth heterogeneities. Separating the competing effects of seismic anisotropy, heterogeneous scattering, and absorption is a tough challenge at the field scale (Fehler 1991; Chapman 2003; Durán *et al.* 2018), particularly in active fault systems (Bianco *et al.* 2005; Napolitano *et al.* 2019; Sketsiou *et al.* 2020). Seismic scattering is efficient at imaging fluid-filled fracture networks (Main *et al.* 1990; Carcione & Picotti 2006); thus, it is increasingly used as a mapping tool for faults (Maercklin *et al.* 2004; Napolitano *et al.* 2019). Heterogeneous scattering increases the duration and complexity of ground motion, even when just a few kilometres away from the epicentre (Imperatori & Mai 2015). In near-source studies, this role has often been disregarded or corrected in an approximate manner (Ripperger *et al.* 2008), using the principle that the wavelength (λ) is much larger than the propagation distance.

Seismic scattering is a crucial marker of increased Earth heterogeneity in the far field, that is when the propagation distance is much larger than λ. Takahashi *et al.* (2007, 2009) and Tripathi *et al.* (2010) developed a tomographic method using the Markov approximation (Saito 2002) to map crustal heterogeneity. The imaging attribute is the time delay between the onset of the wave and the maximum amplitude of seismic energy (the *peak delay*). This maximum can occur at any point within the waveform coda, for

example high amplitude arrivals that occur immediately after the direct wave arrival or at later lapse times. The authors observed spatial correlations of high peak delays with the location of quaternary age volcanoes. Expanding further on the technique, Calvet *et al.* (2013) and Borleanu *et al.* (2017) used high peak delays to mark deformation in the Pyrenees and tectonic processes in Romania, respectively. More recently, Napolitano *et al.* (2019) demonstrated that peak delays, in conjunction with coda attenuation mapping, can reconstruct the complex space-frequency evolution of seismically active fluid-filled fault systems, tracking shorter-scale cross faulting with increasing frequencies. Maps of high peak delays agree well with physical attributes such as fracture patterns that block the lateral migration of fluids across the network This study suggests a potential of frequency-dependent peak delay for imaging and monitoring fracturing- and deformation-related processes using frequency-dependent peak delays within the waveform coda.

Any mapping and monitoring attribute requires well-constrained laboratory calibration to be considered reliable. Data from laboratory experiments suggest that amplitude-dependent attributes, particularly seismic attenuation, can better characterize rock-physics attributes like pore space (Di Martino *et al.* 2021) and fluid type (Adam *et al.* 2009) when paired with seismic phase data. Some experiments have reproduced specific conditions observed in the field to calibrate the ability of attenuation parameters to image fault structures (Tisato & Quintal 2014; Barnhoorn *et al.* 2018). Often used are acoustic emissions (AE), the laboratory analogue to earthquake data, as they provide a window into the near-field scattering regime (Zhang *et al.* 2019).

Rock-physics experiments are already a powerful tool for reproducing deformation and fracturing in porous media under stress conditions that are known and controlled (Harnett *et al.* 2018). As the density of fractures increases, AE waveform data becomes highly sensitive to deformation structure with significant variations in *P*- and *S*-wave velocities (e.g. Schubnel *et al.* 2003). In contrast, active surveys conducted using synthetic media have demonstrated a geometrical bias to scattering parameters due to the relative positioning of heterogeneous structures and the AE acquisition array (Rao & Wang 2009). In simulations of fluid-filled cracks, Ma *et al.* (2022) highlight that phase velocities and dissipation factors have a dependence on the angle of incidence as energy propagates through a medium. Numerical studies identify a dependence of scattering attenuation parameters on frequency, where the inverse quality factor, mapping attenuation, is linearly dependent on fracture density (Vlastos *et al.* 2007; Fang *et al.* 2013). Furthermore, within the early coda of simulated ultrasonic waveforms, Yoshimitsu *et al.* (2016) identified low-frequency, high-amplitude arrivals in cylindrical steel samples. The authors attributed these to surface waves acting after direct wave energy interacted with the sample boundaries.

Shear zones and competent layers represent heterogeneities within a rock mass. In addition to the initial heterogeneity (grain size, mineralogy, porosity and initial crack damage) at the onset of the loading, a rock sample suffers increasing crack damage and stress concentrations. A heterogeneously deformed sample can be divided into three zones: strain-forbidden zone, intensive strain zone and intrusion zone, having precise distributions relative to the pistons and direction of normal stress (Ji & Wang 2011). In the field, peak delays are sensitive to heterogeneity represented by variations in elastic constants and density. In controlled experiments, the final distribution of these quantities is constrained and may be used to investigate the frequency-dependent sensitivity of peak delays.

This study examines the spatial and temporal variation of peak delays measured from AE in a sample of Darley Dale Sandstone (DDS) as an analogue for crustal-scale interfaces observed in the near field and for a high scattering regime. The mechanical behaviour of DDS under conventional triaxial conditions is well reported in the literature (Baud & Meredith 1997; Heap *et al.* 2009; King *et al.* 2021). We conducted several focused experiments to relate the onset and development of cracking to the different deformation stages (i.e. compaction, dilatancy and shear) by analysing the AE recorded by an array of piezoelectric transducers (PZT) as the fault zone structure develops.

This sample set and the generated AE data set have been previously analysed for waveform picking and fracturing source mechanisms (King *et al.* 2020, 2021). Using their data, we focus on frequency and time dependencies of peak delays as a quantity sensitive to medium heterogeneity. Results are analysed and related to a developing fracture network and strain distribution to provide quantitative support for mapping and monitoring faults with the attribute and better understanding the physics underlying their changes. Specifically, we present new methods to:

pick ‘Beyond the Direct Wave’ (BYD) onsets following a time–frequency transformation of the signal (Constant-Q Transform, CQT); calculate the average waveform and dominant frequency content and define the peak delay as the time difference between the BYD onset and the maximum amplitude arrival of energy in the ultrasonic coda; assess the time-dependent coda variations in frequency and amplitude and produce tomographic maps of peak delay.

While the definition is analogous to the one used at the field-scale, the peak delay quantified here is not a measurement of far-field forward scattering modelled by the Markov approximation (e.g. Saito 2002). Our primary hypothesis is that the peak delay measured on AE waveforms is a cumulative parameter that cannot be reduced, even if along the ray path there are weak heterogeneities (Takahashi *et al.* 2007). We discuss the potential of these attributes for monitoring in the field, with particular emphasis on deformation in fault zones. In this first paper of a two-paper set, we focus on the laboratory rock physics aspects of the peak delay analysis. In contrast, a second companion paper presents the theoretical and computational modelling of the inferred processes.

2 DATA AND METHODS

2.1 Material investigated, experimental setup and data acquisition

Known for its homogenous properties, Darley Dale Sandstone (DDS) is a brown-yellow, feldspathic sandstone with a modal composition of quartz (69 per cent), feldspars (26 per cent), clay (3 per cent) and mica (2 per cent). Previous studies report a connected porosity of 13.3 $\pm$ 0.8 per cent, with grain sizes varying from 100 to 800 μm (Heap *et al.* 2009). No distinct layering or laminations are identified in hand sample. The samples used in this study are 4 cm (diameter) $\times$ 10 cm (length) cylinders obtained using a hollow diamond-tipped coring drill with the ends ground flat and parallel to within 0.01 mm (King *et al.* 2020, 2021).

A conventional triaxial deformation cell, installed at the Rock Mechanics Laboratory, University of Portsmouth (e.g. Harnett *et al.* 2018) deformed the sample. For data acquisition, the protocol of Benson *et al.* (2007) was followed. The acquisition setup is summarized in Table 1. The dry sample was positioned inside a rubber FKM-B nitrile jacket in which an array of twelve 1 MHz Nano-30

Table 1. Summary of laboratory acquistion parameters.

Experimental conditions		Data acquisition	
Characteristic	Value	Characteristic	Value
Confining pressure	20 MPa	Sensor model	PAC Nano30
Strain rate	10^{-5} s^{-1}	Frequency sensitivity	1 MHz
Sample dimensions	40 × 100 mm	Flat frequency response	125–750 KHz
Sample shape	Cylinder	Trigger voltage	60 mV
No. of AE sensors	12	Preamplifier	60 dB

(physical acoustics) piezo-electric transducers (PZTs) were embedded. These sensors measure the radial motion of the wavefield. The jacket was then placed inside the deformation cell, and the PZTs were connected to a high-speed digitizer (10 MHz sampling rate) via 60 dB signal pre-amplifiers. Once sealed, the rubber jacket separates the sample from the oil confining medium, generating a confining pressure of 20 MPa ($\sigma_2 = \sigma_3$). Axial stress, σ_1, is applied via a piston at a constant strain rate of 3.6 mm hr^{-1}, a strain rate of approximately 10^{-5} s^{-1}. The sample is deformed until a macroscopic fault zone coalesces at dynamic failure.

2.2 Waveform picking and source location

Triggered AE events were recorded when energy exceeded a minimum threshold of 60 mV at any sensor of the 12-channel array. An ASC Richter system (AE recorder) was used for digitizing the signals. The *P*-wave onsets of recorded AE are picked automatically using a Time Delay Neural Network (TDNN; Waibel *et al.* 1995; Peddinti *et al.* 2015; King *et al.* 2020). A model is trained on time-series of instantaneous frequency (Huang *et al.* 1998), seismic amplitude and permutation entropy (Unakafova & Keller 2013). By applying a binary classification approach of the AE, the waveform can be categorized as either background noise or signal, providing more efficient time-series to pick the onset of energy even at low amplitudes.

A Time Difference of Arrival method (TDOA) is applied to locate the AE epicentres using *P*-wave onsets (Tobias 1976; Comanducci *et al.* 2020). Pairwise subtraction of observed arrival times (a minimum of 6) to each sensor is minimized against calculated arrivals times through iterative estimation of the source location. The L2 norm (sum of squared misfits) arrives at a local minimum at the source location with a maximum estimated error of 2 mm. In post-deformation imagery, simple surface expressions of fractures highlight newly formed fault zone structure dipping 60° to the left following sample failure (dashed red line, Fig. 1a). Enhanced X-ray Computed Tomography highlights the single failure plane illuminated from the northwest (Fig. 1b). We note that this is not a perfectly planar feature, deviating from a flat surface by approximately 4 mm in either direction. PZT receivers (diamonds), source locations (black circles) and straight ray paths (grey lines) indicate that the AE waveforms have extensively sampled the deformation structure (Fig. 1c).

The source mechanism could dominate the waveform and thus peak delays at such small hypocentral distances. For example, variations in frequency content have been previously used for source classification (Ohtsu *et al.* 2002). In addition, discrepancies in the attenuation properties of tensile events have been related to the orientation of the fault (Kwiatek & Ben-Zion 2013). Following the methodology of King *et al.* (2021), the radiation patterns of AE were classified to determine source-specific variations character and frequency content. Fracturing mechanisms fall within a range of distributions whose extremes are pure compaction (C-type), pure shear (S-type) and pure tension (T-Type; Frohlich *et al.* 2016; King *et al.* 2021).

Near-source scattering results in increased complexity of the direct wave energy when an event occurs close to a boundary or discontinuity (Lacanna & Ripepe 2013); in this case, strong *P*-wave reflections can modify early *S*-wave amplitudes. Unclear *S*-wave onsets were picked automatically, following a time–frequency transformation of the signal (Constant-Q Transform, CQT). The CQT is a technique that transforms a time-domain signal into the time–frequency domain with non-stationary Gabor frames. The centre frequencies of the frequency bins are logarithmically spaced, and their Q-factors are all equal. It is essentially a wavelet transform with a higher potential resolution than conventional techniques (12–96 bins per octave). The Q-factor of bin k is defined $Q_k = \frac{f_k}{\Delta f_k} = \frac{N_k f_k}{\Delta \omega f_s}$, where f_k, Δf_k and $\Delta \omega f_s$ denote the centre frequency, the –3 dB bandwidth of the frequency response and the –3 dB bandwidth of the main lobe of the spectrum of the window function, respectively (Schörkhuber & Klapuri 2010). The window length N_k is inversely proportional to f_k to have the same Q-factor for each bin. After computing the highest octave Q-factors over the entire signal, the input is low-pass filtered and downsampled by a factor of 2 to repeat the calculation for the desired number of octaves (Schörkhuber & Klapuri 2010). The *S*-wave onset is then defined as a local minimum in the CQT of the waveform bandpass filtered between 300 and 600 kHz, occurring shortly after the first pulse of the *P* wave. Due to the near-source scattering effects, it is not reliable to separate reflected *P*-wave energy from the *S* wave; therefore, this onset is defined as 'Beyond the Direct Wave' (BYD).

2.3 AE source mechanisms, ray paths and waveforms

Only the first arriving waveform for AE is considered to determine what waveform attributes are related to the source (Fig. 2). These typically only travel 1–2 cm before reaching a receiver. Waveforms were selected from AE located within 12.5 mm of each other (approximately one wavelength at 200 kHz) and that occurred within a 2-min window. This selection minimized the influence of time-varying structures whilst ensuring a representative from each mechanism type (Fig. 2, columns 2–4). Waveforms are presented with corresponding ray paths (Fig. 2, column 1, coloured lines) and the CQT that defines the BYD onset (Fig. 2, columns 2–4, red line). Vertical black lines indicate *P* wave and estimated BYD arrivals.

Individual waveforms for each mechanism are averaged together and are presented with the bootstrapped modal frequency content (Hilbert transform, Fig. 3, bottom row). The grey regions indicate the standard deviation (1 std and 1/5 std) of the bootstrapped time-series, and n is the number of waveforms. Vertical black bars indicate the average *P* wave and BYD arrival times. Here, the BYD shows an approximate 30 kHz reduction in dominant frequency content, regardless of mechanism type (Fig. 3, top row). The three mechanisms produce small differences in the BYD estimation and, therefore, the corresponding peak delay measurement.

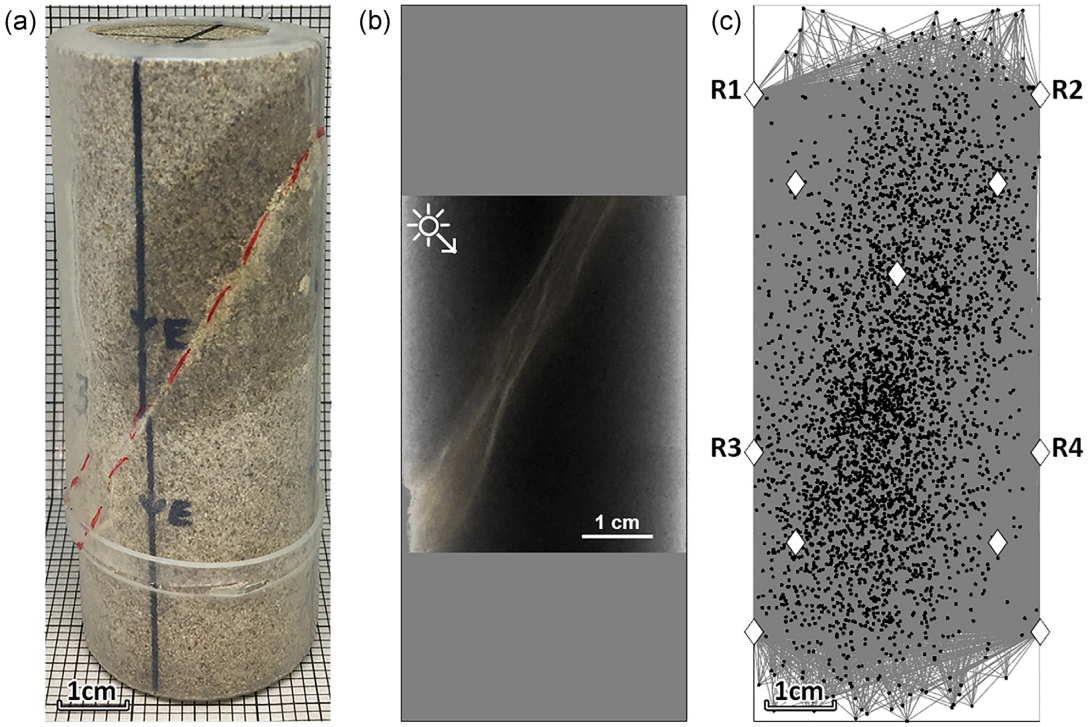

Figure 1. (a) Post-deformation imagery highlight surface expressions of fault zone structure (red line). (b) Enhanced 3D X-Ray Computed Tomography of the deformed sample with the fault surface highlighted from the northwest. It is not perfectly planar and deviates from a flat surface by up to 4 mm in either direction. The bounding box indicates sample boundaries. (c) Source locations (black dots), ray paths (assumed straight, grey lines) and receiver array geometry (diamonds). A high number of AE occur near the fault and may bias imaging.

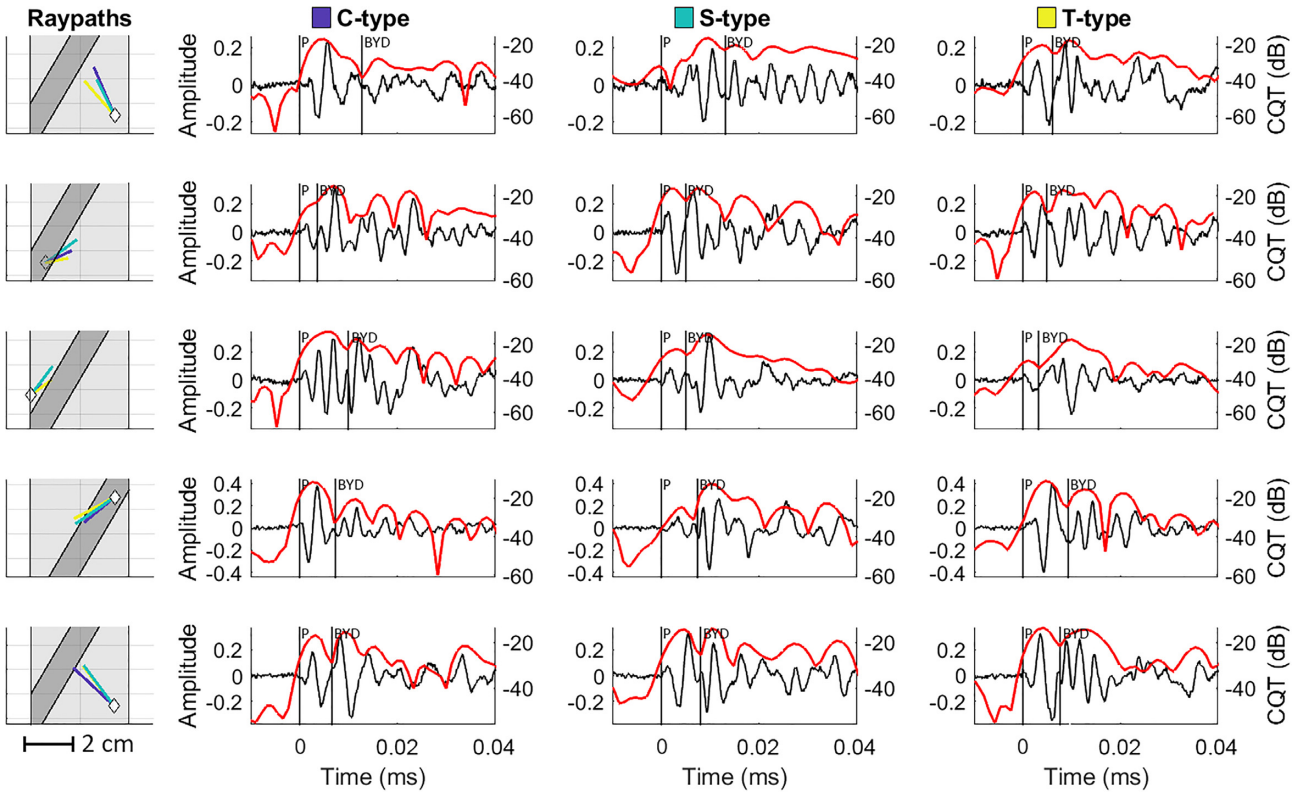

Figure 2. Example waveforms for each mechanism type (columns) occurring close to each other in space and time (rows). The first column indicates ray paths (coloured lines corresponding to mechanism type) of events to a receiver (diamond). A dark grey region is used to indicate the fault zone. Waveforms are presented with their corresponding Constant-Q Transform (red line), used to estimate the 'beyond the direct wave' onset.

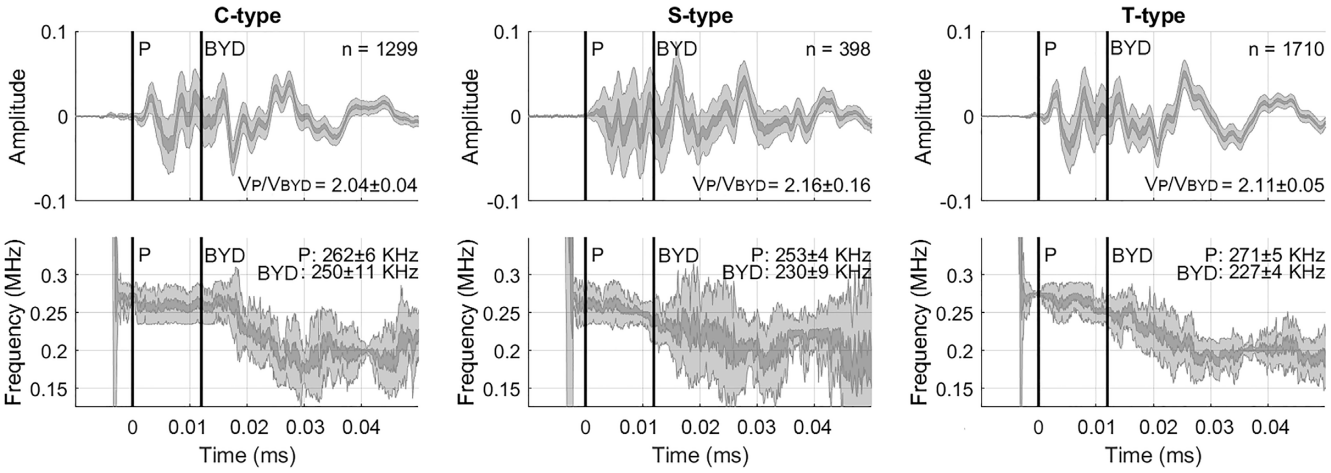

Figure 3. Average waveform and dominant frequency content for *n* waveforms. Vertical bars indicate average *P* wave and BYD onsets for DDS.

2.4 Measuring peak delay at the laboratory scale

Relative to the field scale, laboratory media show higher levels of heterogeneity. Consequently, scattering might evolve from the Rayleigh (at low frequencies) to the Mie (at higher frequencies) scattering regime. Therefore, peak delays were measured on waveforms filtered in two frequency bands: 0.05–0.5 MHz and 0.5–1 MHz. Assuming a typical *S*-wave velocity of 2.3 km s^{-1} (Heap *et al.* 2009), this corresponds to wavelengths of 44.6 mm (0.05 MHz), 4.5 mm (0.5 MHz) and 2.2 mm (1 MHz). The low-frequency observations thus fall within the near-field Rayleigh scattering, while the high frequencies are dominated by far-field Mie scattering. This difference is important, as the radiation lobe due to Mie scattering is much stronger in the forward direction and could lead to direction-specific effects due to source–receiver geometry. Peak delays are therefore expected to show different sensitivity to heterogeneity depending on frequency.

A generalized definition of the relative variation of peak delay is proposed in Takahashi *et al.* (2007) to account for a traveltime dependence that occurs at the far-field. However, De Siena *et al.* (2016) noted that high uncertainties affect the coefficients obtained in the proposed linear model, and the fit is imprecise for short hypocentral distances. Further, Zhang *et al.* (2019) concluded that the traditional exponential function models of attenuation laws are insufficient to describe the amplitude losses of AE waves in the near field. Therefore, unlike field-scale studies, we do not consider the influence of hypocentral distances in this study. A peak delay is defined here as the time difference between the BYD onset and the maximum amplitude arrival of energy in the coda, to minimize the influence of source/near-source effects. Each signal is filtered in the target frequency band, from which the RMS envelope is calculated (Fig. 4). Envelopes are smoothed over a 0.005 ms window. Hereafter, peak delay is considered as the relative value $\Delta \log(\mathrm{PD}_f)$ that varies around the average of all (*n* number) measurements for each frequency band (*f*):

$$\Delta \log\left(\mathrm{PD}_f\right) = \log\left(\mathrm{PD}_f\right) - \frac{1}{n}\sum_{i=1}^{n} \log\left(\mathrm{PD}_f\right).$$

A small $\Delta\log(\mathrm{PD}_f)$ marks the absence of high heterogeneity along the ray path while the opposite is true for high values.

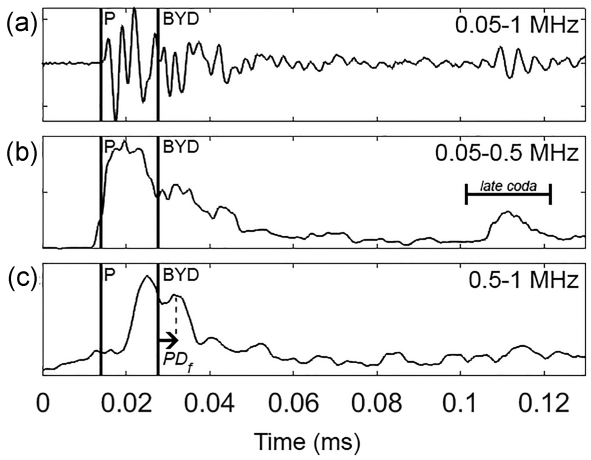

Figure 4. Example of observed AE and its envelopes. (a) Displacement voltage waveform in 0.05–1 MHz band. *P* wave and BYD onsets are indicated. (b) RMS envelope at 0.05–0.5 MHz. A late coda arrival occurs for many waveforms between 0.1 and 0.12 ms. (c) RMS envelope at 0.5–1 MHz. PD_f is the peak delay time from the BYD onset.

3 RESULTS

We present the changes in AE data amplitude, frequency, and peak delay in Fig. 5. On the left-hand side, we show the probability of detecting AE data of different types during the experiment for different receivers and azimuths (rows). The AE waveforms are categorized according to (1) frequency and (2) amplitude contents in the late coda as either *high* or *low*. The threshold is at 50 per cent of the range for each parameter (i.e. frequency or amplitude) throughout the experiment. Thus, we can define four groups: (1) low frequency, low amplitude coda (LF-LA), (2) low frequency, high amplitude coda (LF-HA), (3) high frequency, low amplitude coda (HF-LA) and (4) high frequency, high amplitude coda (HF-HA). For each category, a probability density function (PDF) is calculated for the time of occurrence of individual waveforms as a function of time. All four PDFs are then summed together, and a percentage contribution is calculated (King *et al.* 2021).

When considering arrivals to the PZT receivers located orthogonal to the fault plane (Fig. 5a), the first half of the experiment is dominated by LF energy, likely related to the generation of surface

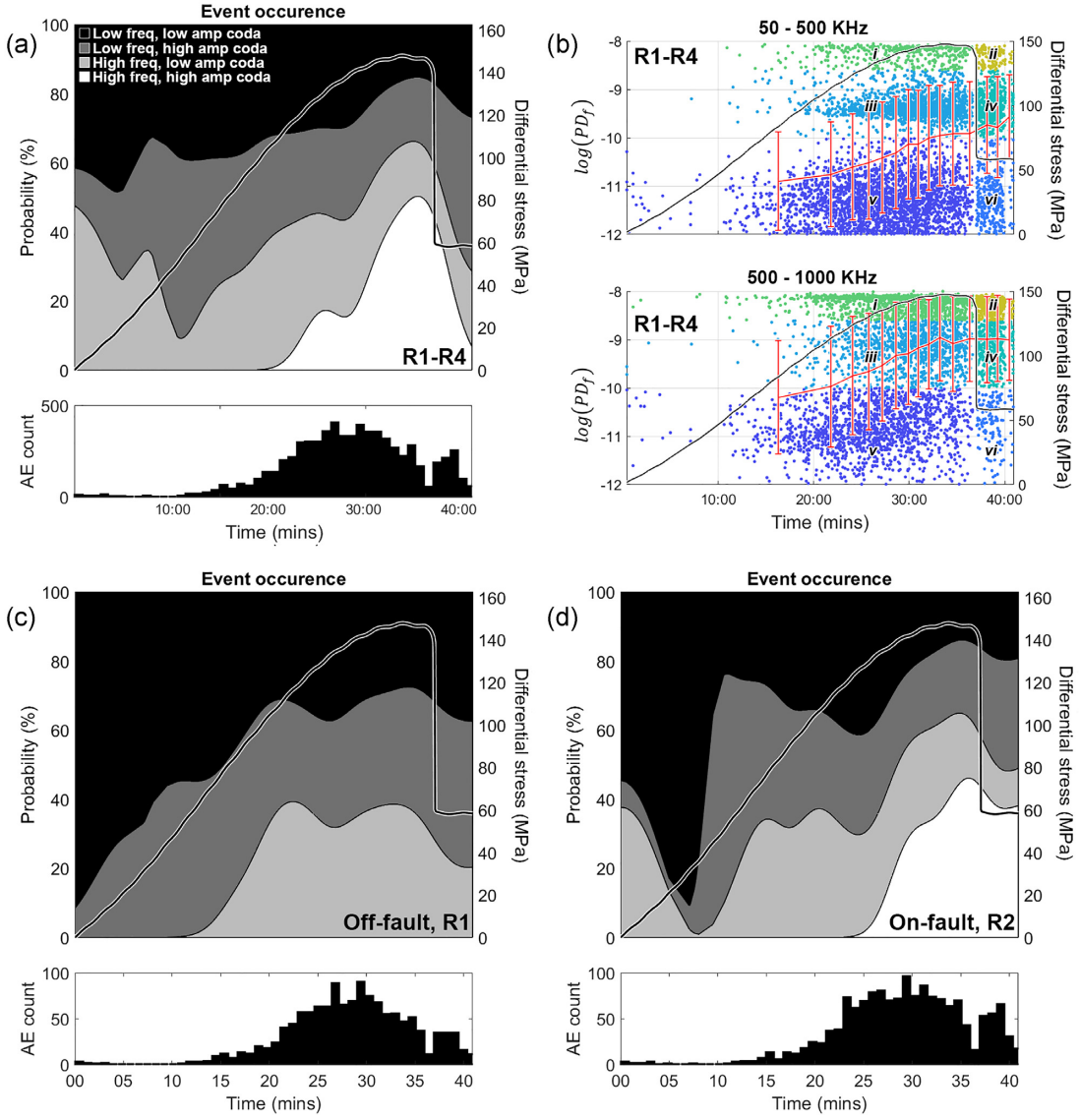

Figure 5. Comparisons of waveform properties with differential stress recorded during the experiment. Crack closure between 0 and 10 min. Fracture nucleation and growth between 10 and 25 min. Fault coalescence between 25 and 32 min. Ultimate compressive stress and onset of dynamic failure (stress drop) from 32 min. (a) Time-dependent variations in frequency and amplitude content of the AE coda for arrivals to orthogonal receivers R1–R4. Top panel show (1) the probability, or ratio, of the four groups relative to total; (2) histogram counts of AE data. (b) $\log(\mathrm{PD}_f)$ for the analysed frequency bands. Trends (red line) calculated as the average in a moving window of 500 measurements. Error bars are the standard deviation of those measurements. Points are coloured to highlight three main families (for before/after failure) of peak delay values. Group 1 (v and vi): $-12 < \log(\mathrm{PD}_f) < -10$. Group 2 (iii and iv): $-10 < \log(\mathrm{PD}_f) < -8.75$. Group 3 (i and ii): $-8.75 < \log(\mathrm{PD}_f) < -8$. (c) Time-dependent variations in frequency and amplitude content of the AE coda for arrivals to off-fault receiver R1. (d) Time-dependent variations in frequency and amplitude content of the AE coda for arrivals to on-fault receiver R2.

waves from the sample boundaries (Yoshimitsu *et al.* 2016). A family of HF-LA events rapidly reduces in probability from >40 per cent to almost <5 per cent during the first 10 min. After this time, HF events steadily increase as new fractures nucleate. As the fault zone begins to coalesce at ∼25 min, the number of AE rapidly increases, and a new group of HF-HA events starts to dominate. These events have an occurrence likelihood of >40 per cent at sample failure. These waveforms arrive primarily to the on-fault receiver (Fig. 5d) with little-to-no arrivals for the off-fault station (Fig. 5c). These amplitude variations are reflected in the peak delay, where a gradual increase is observed for both frequency bands as the experiment progresses. Trends are calculated as the moving average within a window of 500 measurements. At low frequencies (Fig. 5b, top) the trend is almost linear. While at high frequencies (Fig. 5b, bottom), the trend flattens as the sample reaches its ultimate compressive stress at 150 MPa, shortly before dynamic failure.

Three dominant groups of peak delay can be observed (Fig. 5b, coloured points and corresponding coloured waveforms in Fig. 6). These are further separated for before and failure (experimental time 35 min). Waveforms from each group are averaged together (with zero time-shift) and then bandpass filtered within the two analysed frequency bands. Fig. 6(a-ii) shows the time distribution of the different peak delay groups relative to arrivals in the AE waveform. All groups highlight a relative increase in peak amplitudes following

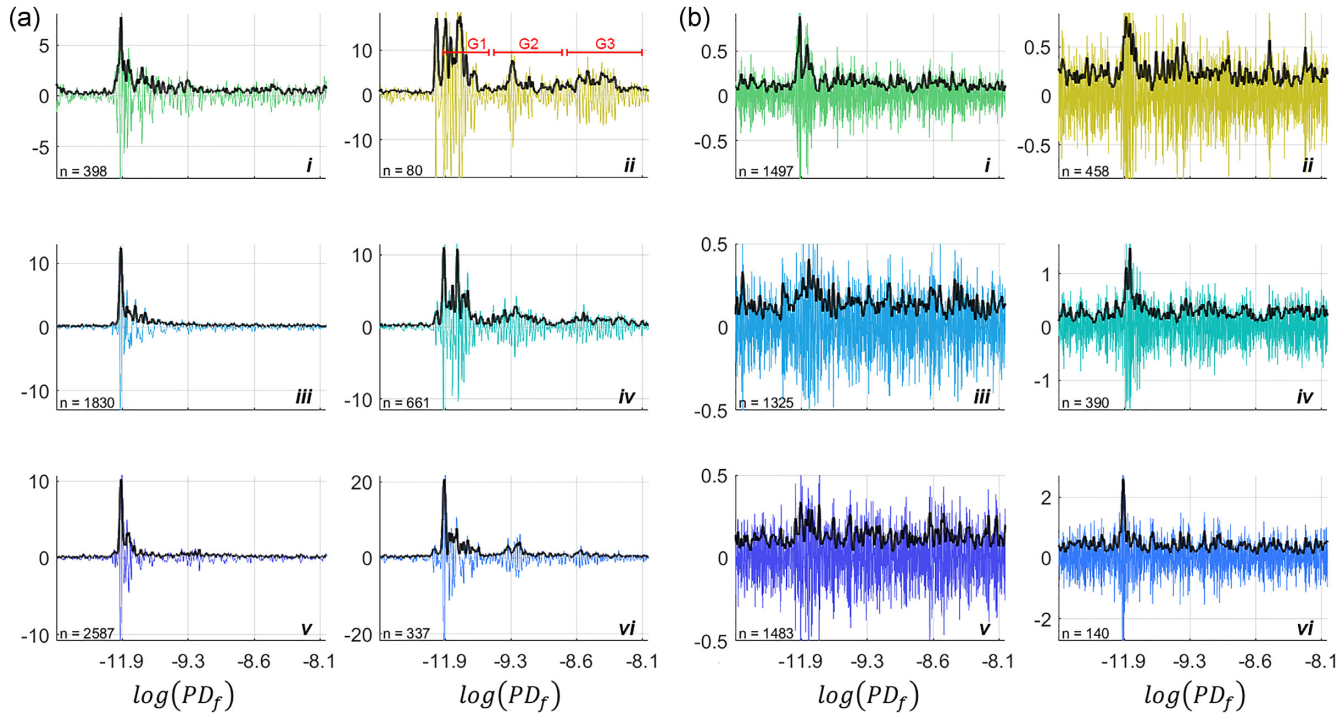

Figure 6. Waveforms for corresponding coloured groups in Fig. 5(b) are averaged together and then bandpass filtered for a) 50–500 KHz and (b) 500–1000 KHz. Waveforms are coloured to highlight three main families (for before/after failure) of peak delay values. Group 1 (G1, v and vi): $-12 < \log(\mathrm{PD}_f) < -10$. Group 2 (G2, iii and iv): $-10 < \log(\mathrm{PD}_f) < -8.75$. Group 3 (G3, i and ii): $-8.75 < \log(\mathrm{PD}_f) < -8$. Labels G1 to G3 in (a-ii) show the time distribution of the different peak delay groups relative to arrivals in the waveform.

dynamic failure. In detail, Group 1 [G1, $-12 < \log(\mathrm{PD}_f) < -10$] demonstrate strongly impulsive direct wave arrivals with little-to-no arrivals in the coda beyond the BYD (e.g. Fig. 6a, bottom left). Group 2 [G2, $-10 < \log(\mathrm{PD}_f) < -8.75$; e.g. Fig. 6b, centre left] and Group 3 [G3, $-8.75 < \log(\mathrm{PD}_f) < -8$; e.g. Fig. 6b, top right] typically have reduced amplitude and an increased broadening of the direct wave. Relative coda wave amplitudes are higher than in G1 for both groups.

In analogy to field-scale tomography, the medium is discretized into model blocks (5 × 5 × 5 mm in size) to obtain an image of the interior of the sample. The model is orientated so that the grid bisects the fault at an orthogonal angle. Each block is assigned the average $\Delta\log(\mathrm{PD}_f)$ of all the ray paths that cross it to minimize time-dependent effects (De Siena *et al.* 2016). For this analysis all 12 PZT receivers are used. Source–receiver pathways are then assigned their measured peak delays. Only blocks crossed by a minimum of 5 rays are solved to minimize anomalous variations in regions of low path coverage. Peak delay values are smoothed at a block by averaging each block-value with blocks within 5 mm distance. The 3-D distribution of anomalies is then 'depth-averaged' along the fault strike to create a 2-D map. Although this approach limits the detection of minor anomalies, it ensures that major structures are adequately sampled from all directions.

Low-frequency observations show no clear signature of the post-deformation fault zone (Fig. 7, left). The primary positive peak-delay anomaly underlines the left-hand side of the sample in both frequency bands (Fig. 7). A similar anomaly is expected at these frequencies, as the sample boundaries produce surface waves generated by multiple scattering that propagate vertically (Yoshimitsu *et al.* 2016). The difference in peak intensity is likely related to the proximity of the largest seismicity cluster to the left-hand side of

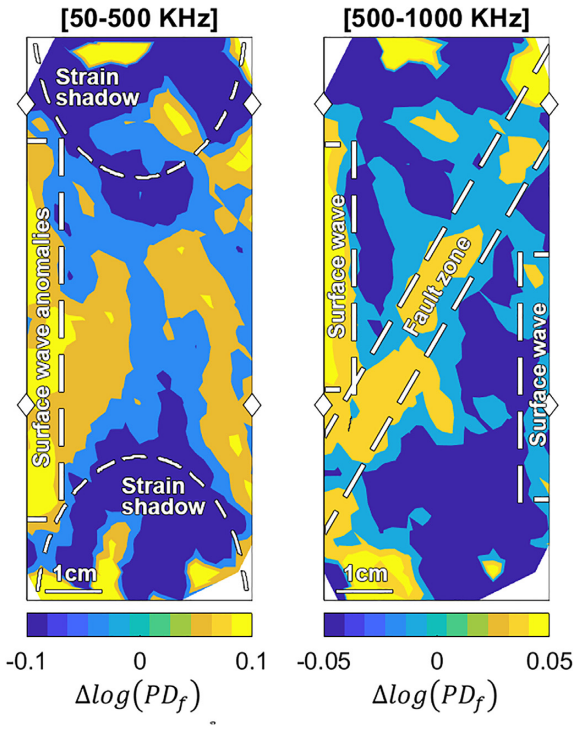

Figure 7. Distribution of logarithmic variations of BYD [$\Delta\log(\mathrm{PD}_f)$] obtained using all 12 receivers. The bounding box indicates sample boundaries. Receivers R1–R4 are shown as diamonds.

the sample (Fig. 1c). The result is an increase in the number and energy of reverberating waves. Although the distribution of anomalies suggests strain-forbidden zones at 0.05–0.5 MHz (e.g. Ji & Wang

2011), there are biases imposed by the distribution of AE along the fault zone and under-sampling of these areas.

The fault-zone is visible as a central, left-dipping region of positive $\Delta\log(\mathrm{PD}_f)$ anomalies in the 0.5–1 MHz map (Fig. 7, right). These anomalies appear to 'thicken' towards the lower half of the fault zone, likely due to the observed undulations of the fault surface (Fig. 1b). Likely, the high values of $\Delta\log(\mathrm{PD}_f)$ present along the radial boundaries are again related to surface waves from waveforms that travel along the sample edges (Yoshimitsu *et al.* 2016). These anomalies are approximately one wavelength in thickness and are similar in magnitude to those produced by the fault zone.

4 DISCUSSION

In regions of strong deformation, the delay in the maximum arrival of seismic energy has been observed to correlate strongly with the distribution of heterogeneity in the lithosphere (Takahashi *et al.* 2007; De Siena *et al.* 2016; Napolitano *et al.* 2019). By adopting standard approaches of scattering (peak delay) tomography, the results presented here suggest that similar processes may occur at the laboratory scale. They highlight a clear potential for AE-led studies to calibrate time-dependent scattering structures like active fault zones (Fig. 5). Unlike seismic data, which typically sample structures that may change over a few decades (Napolitano *et al.* 2019), the nature of the laboratory setup results in significant structural variations that can occur over seconds (Benson *et al.* 2010).

Uncertainties in the frequency characteristics of the source require a preliminary characterization of the source processes (Fig. 4). Whilst pure shear-type events are likely in the minority (McBeck *et al.* 2019; Renard *et al.* 2019), the source classification routine applied here does not fully account for the frequency drop associated with individual components of shear within dominantly tensile events (King *et al.* 2021). We have applied large frequency windows and an automated routine to target energies that arrive after the direct wave to minimize such effects on our observations (Fig. 2).

The low-frequency image replicates: (1) the expected cone-shaped strain-forbidden zones near the pistons where practically no crystal plastic deformation occurs as low peak delays and (2) the combined intense strain and intrusion zones of high and average deformation (Fig. 7). These zones are expected for viscosity ratios as small as ten between inclusions and surrounding material (Moulas *et al.* 2014), which is certainly the case in our experiment. However, Yoshimitsu *et al.* (2016) carried out an experiment on undeformed, homogeneous aluminium samples, suggesting that surface waves from the sample boundaries could dominate the maps obtained at low frequencies. The variations in the late waveform coda for individual AE do at least confirm the occurrence of LF-HA arrivals from approximately 0.1 ms after the *P* wave (Fig. 4). We will investigate the origin of these arrivals in the companion paper (this volume, K22B). Future experiments on different lithologies, size or experimental conditions could confirm that peak delays are sensitive to deformation-induced heterogeneity in this frequency band and at this scale, even if they have no resolution on the shear zone. This confirmation is essential to poorly resolved structures, as it is the case for the metamorphic processes triggered by increasing heterogeneity and imaged by the seismic response (Moulas *et al.* 2014; Cioniu *et al.* 2019).

Less uncertainty affects the high-frequency imaging, where the shear zone is visible as high peak delays. Pore space topology alone can play an essential role in increasing peak delays of high-frequency waveforms (Di Martino *et al.* 2021); therefore, similar mechanisms likely occur in this fractured fault-driven system. We further investigate this relationship between frequency and fault structure in the companion study (this volume, K22B). Despite the limitations in observation geometry, the maps in Fig. 7 indicate that peak delays can map strain-related structures (Fig. 1).

The time-dependent results indicate that the mapped features are time-dependent, like in field-scale fault zones (Napolitano *et al.* 2019; Qiu *et al.* 2020). In Fig. 5, we observe a dominance of higher-frequency energy within the coda window as the fault zone coalesces. For on-fault stations, this is driven by a relative increase in the number of HF arrivals in the coda, leading to higher peak delays at higher frequencies (Fig. 5b). Resonance in the Mie scattering regime (Di Martino *et al.* 2021) is an attractive explanation for the occurrence of high frequency trapped waves arriving at late lapse times in the AE data (e.g. Fig. 6b, G3). Indeed, trapped waves are related to field-scale deformation structure (e.g. Qiu *et al.* 2020; Roy *et al.* 2020), and power density spectra analysis has shown that waveforms maintain larger amplitudes and longer wave trains at seismic stations closer to the Longmen Shan fault zone (Huang *et al.* 2020). The differences between G2 and G3 could be indicative of different scattering regimes whereby fault zone trapped arrivals begin to dominate waveforms at late lapse times for stations on or near the fault.

Our results provide a laboratory-scale calibration to observations made in the field. Nonetheless, due to limitations in sampling and the complexity of the data, a time-dependent peak delay tomography remains impractical. However, a proxy can be realized through numerical simulations of wavefield propagation that assess the different stages of deformation and rupture in fault zones. We perform this numerical analysis in the companion study of this two-paper set (this volume, K22B). Observed waveforms from the laboratory experiment are used as a target to fit model parameters of elastic moduli seismic Q and strain distribution during the early phases of deformation and shortly following the dynamic failure of the sample. By linking scattering and dissipation parameters to rough faulting, distributed weakening, and off-fault deformation (Griffith *et al.* 2010; Renard *et al.* 2019), this approach could pave the way for the use of scattering and absorption attributes beyond mapping, for example to monitor regions of expected rupture.

5 CONCLUSIONS

We developed AE experiments in DDS to test the sensitivity of peak delay, a known proxy of seismic scattering at the field scale, to deformation-induced structures, strain, and rheological heterogeneities. We map peak delays in space, obtaining tomographic maps in low (50–500 kHz) and high (500 kHz–1 MHz) frequency ranges. The results show that peak delays are sensitive to surface waves developing across the boundaries of the sample; however, depending on frequency, they are also sensitive to primary, known spatial variations in heterogeneity and strain. At low frequency, the resolution is sufficient to map differences in strain caused by the heterogeneity of the sample, which is progressively increasing. At high frequencies, peak delays detect the zone of intense strain corresponding to the post-deformation shear zone. Temporal analysis confirms a dependence of peak delay properties on the different stages of deformation. However, the trends depend on the position of source and sensor, with high frequency peak delays occurring at sensors in contact with the coalescing fault during dynamic failure.

Peak delays are essential for assessing earthquake source characteristics and are now used for imaging the heterogeneous Earth

in combination with coda parameters, specifically coda attenuation. The sensitivity to heterogeneity, strain, and fracturing, shown by peak delay imaging and temporal variations is key for assessing their potential for mapping damage in the Earth's crust. The results presented here provide invaluable constraints to interpret field-scale parameters. Together with our companion modelling paper, which offers necessary physical explanations to our results, the present work has important implications for field-scale measurements and imaging of scattering parameters, especially in the near-source high-scattering regime.

DATA AVAILABILITY

Acoustic Emission data are obtained at the Rock Mechanics Laboratory, University of Portsmouth. The data underlying this article are available in Zenodo, at https://doi.org/10.5281/zenodo.3958910. Programming codes were developed in MATLAB ® version 2018a.

CONFLICT OF INTEREST

All authors declare that they have no conflicts of interest.

REFERENCES

Adam, L., Batzle, M., Lewallen, K. T. & van Wijk, K., 2009. Seismic wave attenuation in carbonates, *J. geophys. Res.,* **114**(B6), doi:10.1029/2008JB005890.

Barnhoorn, A., Verheij, J., Frehner, M., Zhubayev, A. & Houben, M., 2018. Experimental identification of the transition from elasticity to inelasticity from ultrasonic attenuation analyses: attenuation and the onset of inelasticity, *Geophysics,* **83**(4), MR221–MR229.

Baud, P. & Meredith, P., 1997. Damage accumulation during triaxial creep of Darley Dale sandstone from pore volumometry and acoustic emission, *Int. J. Rock Mech. Min. Sci.,* **34**(3–4), 24–e1.

Benson, P. M., Thompson, B. D., Meredith, P. G., Vinciguerra, S. & Young, R. P., 2007. Imaging slow failure in triaxially deformed Etna basalt using 3D acoustic-emission location and X-ray computed tomography, *Geophys. Res. Lett.,* **34**(3),

Benson, P. M., Vinciguerra, S., Meredith, P. G. & Young, R. P., 2010. Spatio-temporal evolution of volcano seismicity: a laboratory study, *Earth planet. Sci. Lett.,* **297**(1–2), 315–323.

Bianco, F., Pezzo, E. D., Malagnini, L., Luccio, F. D. & Akinci, A., 2005. Separation of depth-dependent intrinsic and scattering seismic attenuation in the northeastern sector of the Italian Peninsula, *Geophys. J. Int.,* **161**(1), 130–142.

Borleanu, F., De Siena, L., Thomas, C., Popa, M. & Radulian, M., 2017. Seismic scattering and absorption mapping from intermediate-depth earthquakes reveals complex tectonic interactions acting in the Vrancea region and surroundings (Romania), *Tectonophysics,* **706-707,** 129–142.

Calvet, M., Sylvander, M., Margerin, L. & Villaseñor, A., 2013. Spatial variations of seismic attenuation and heterogeneity in the Pyrenees: coda Q and peak delay time analysis, *Tectonophysics,* **608,** 428–439.

Carcione, J. M. & Picotti, S., 2006. P-wave seismic attenuation by slow-wave diffusion: effects of inhomogeneous rock properties, *Geophysics,* **71**(3), O1–O8.

Chapman, M., 2003. Frequency-dependent anisotropy due to meso-scale fractures in the presence of equant porosity, *Geophys. Prospect.,* **51**(5), 369–379.

Cionoiu, S., Moulas, E. & Tajčmanová, L., 2019. impact of interseismic deformation on phase transformations and rock properties in subductions zone, *Sci. Rep.,* **9**(1), 1–6.

Comanducci, L., Cobos, M., Antonacci, F. & Sarti, A., 2020. Time difference of arrival estimation from frequency-sliding generalized cross-correlations using convolutional neural networks, in *ICASSP 2020-2020 IEEE International Conference on Acoustics, Speech and Signal Processing (ICASSP),* pp. 4945–4949, IEEE.

De Siena, L., Calvet, M., Watson, K. J., Jonkers, A. R. T. & Thomas, C., 2016. Seismic scattering and absorption mapping of debris flows, feeding paths, and tectonic units at Mount St. Helens volcano, *Earth planet. Sci. Lett.,* **442,** 21–31.

Di Martino, M. D. P., De Siena, L., Healy, D. & Vialle, S., 2021. Petro-mineralogical controls on coda attenuation in volcanic rock samples, *Geophys. J. Int.,* **226**(3), 1858–1872.

Durán, E. L., van Wijk, K., Adam, L. & Wallis, I. C., 2018. Separating intrinsic and scattering attenuation in full waveform sonic logging with radiative transfer theory, *Geophys. J. Int.,* **213**(2), 757–769.

Fang, X., Fehler, M., Chen, T., Burns, D. & Zhu, Z., 2013. Sensitivity analysis of fracture scattering, *Geophysics,* **78**(1), T1–T10.

Fehler, M., 1991. Numerical basis of the separation of scattering and intrinsic absorption from full seismogram envelope. A Monte-Carlo simulation of multiple isotropic scattering, *Pap. Meteorol. Geophys.,* **42**(2), 65–91.

Frohlich, C., DeShon, H., Stump, B., Hayward, C., Hornbach, M. & Walter, J. I., 2016. A historical review of induced earthquakes in Texas, *Seismol. Res. Lett.,* **87**(4), 1022–1038.

Griffith, W. A., Nielsen, S., Di Toro, G. & Smith, S. A., 2010. Rough faults, distributed weakening, and off-fault deformation, *J. geophys. Res.,* **115**(B8), doi:10.1029/2009JB006925.

Harnett, C. E., Benson, P. M., Rowley, P. & Fazio, M., 2018. Fracture and damage localization in volcanic edifice rocks from El Hierro, Stromboli and Tenerife, *Sci. Rep.,* **8**(1),.

Heap, M. J., Baud, P., Meredith, P. G., Bell, A. F. & Main, I. G., 2009. Time-dependent brittle creep in Darley Dale sandstone, *J. geophys. Res.,* **114**(B7), doi:10.1029/2008JB006212.

Huang, N. E. *et al.*, 1998. The empirical mode decomposition and the Hilbert spectrum for nonlinear and non-stationary time series analysis, *Proc. R. Soc. Lond., A,* **454**(1971), 903–995.

Huang, Y., Li, H., Liu, X., Zhang, Y., Liu, M., Guan, Y. & Su, J., 2020. The multiscale structure of the Longmen Shan Central Fault Zone from local and teleseismic data recorded by short-period dense arrays, *Bull. seism. Soc. Am.,* **110**(6), 3077–3087.

Imperatori, W. & Mai, P. M., 2015. The role of topography and lateral velocity heterogeneities on near-source scattering and ground-motion variability, *Geophys. J. Int.,* **202**(3), 2163–2181.

Ji, S. & Wang, Q., 2011. Interfacial friction-induced pressure and implications for the formation and preservation of intergranular coesite in metamorphic rocks, *J. Struct. Geol.,* **33**(2), 107–113.

King, T., Benson, P., De Siena, L. & Vinciguerra, S., 2020. Acoustic emission waveform picking with time delay neural networks during rock deformation laboratory experiments, *Seismol. Res. Lett.*.**92,** 923–932.

King, T., Vinciguerra, S., Burgess, J., Benson, P. & Siena, L. D., 2021. Source mechanisms of laboratory earthquakes during fault nucleation and formation, *J. geophys. Res.,* **126**(5), e2020JB021059,.

Kwiatek, G. & Ben-Zion, Y., 2013. Assessment of P and S wave energy radiated from very small shear-tensile seismic events in a deep South African mine. *J. geophys. Res.,* **118**(7), 3630–3641.

Lacanna, G. & Ripepe, M., 2013. Influence of near-source volcano topography on the acoustic wavefield and implication for source modeling, *J. Volc. Geotherm. Res.,* **250,** 9–18.

Ma, R., Ba, J.,Carcione, J.M. & Lebedev, M., 2022. P-wave scattering by randomly distributed aligned cracks in fractal media. *Geophysical Journal International* **229,**900–914.

Maercklin, N., Haberland, C., Ryberg, T., Weber, M. & Bartov, Y., 2004. Imaging the Dead Sea Transform with scattered seismic waves, *Geophys. J. Int.,* **158**(1), 179–186.

Main, I. G., Peacock, S. & Meredith, P. G., 1990. Scattering attenuation and the fractal geometry of fracture systems, *Pure appl. Geophys.,* **133**(2), 283–304.

McBeck, J., Kandula, N., Aiken, J. M., Cordonnier, B. & Renard, F., 2019. Isolating the factors that govern fracture development in rocks throughout dynamic in situ X-ray tomography experiments, *Geophys. Res. Lett.*.**46,** 11 127–11 135,

Moulas, E., Burg, J. P. & Podladchikov, Y., 2014. Stress field associated with elliptical inclusions in a deforming matrix: mathematical model and implications for tectonic overpressure in the lithosphere, *Tectonophysics,* **631,** 37–49.

Napolitano, F., De Siena, L., Gervasi, A., Guerra, I., Scarpa, R. & La Rocca, M., 2019. Scattering and absorption imaging of a highly fractured fluid-filled seismogenetic volume in a region of slow deformation, *Geosci. Front.,* **11,** 989–998.

Ohtsu, M., Uchida, M., Okamoto, T. & Yuyama, S., 2002. Damage assessment of reinforced concrete beams qualified by acoustic emission, *Struct. J.,* **99**(4), 411–417.

Peddinti, V., Chen, G., Manohar, V., Ko, T., Povey, D. & Khudanpur, S., 2015. JHU ASpIRE system: robust LVCSR with TDNNS, iVector adaptation and RNN-LMS, in *2015 IEEE Workshop on Automatic Speech Recognition and Understanding (ASRU),* pp. 539–546, IEEE.

Qiu, H., Allam, A. A., Lin, F.-C. & Ben-Zion, Y., 2020. Analysis of fault zone resonance modes recorded by a dense seismic array across the San Jacinto Fault Zone at Blackburn Saddle, *J. geophys. Res.,* **125**(10), e2020JB019756.

Rao, Y. & Wang, Y., 2009. Fracture effects in seismic attenuation images reconstructed by waveform tomography. *Geophysics,* **74**(4), R25–R34.

Renard, F., McBeck, J., Kandula, N., Cordonnier, B., Meakin, P. & Ben-Zion, Y., 2019. Volumetric and shear processes in crystalline rock approaching faulting, *Proc. Natl. Acad. Sci.,* **116**(33), 16 234–16 239.

Ripperger, J., Mai, P. M. & Ampuero, J.-P., 2008. Variability of near-field ground motion from dynamic earthquake rupture simulations, *Bull. seism. Soc. Am.,* **98**(3), 1207–1228.

Roy, N., Mukherjee, S. & Sahu, R. B., 2020. Influence of trapped soft/stiff soil layer in seismic site response analysis, *J. Earth Syst. Sci.,* **129**(1), 1–19.

Saito, T., 2002. Envelope broadening of spherically outgoing waves in three-dimensional random media having power law spectra, *J. geophys. Res.,* **107**(B5),.

Schörkhuber, C. & Klapuri, A., 2010. Constant-Q transform toolbox for music processing, in *Proceedings of the 7th Sound and Music Computing Conference,* Barcelona, Spain, pp. 3–64.

Schubnel, A., Nishizawa, O., Masuda, K., Lei, X. J., Xue, Z. & Guégen, Y., 2003. Velocity measurements and crack density determination during wet triaxial experiments on Oshima and Toki Granites, *Pure appl. Geophys.,* **160**(5), 869–887.

Sketsiou, P., Napolitano, F., Zenonos, A. & De Siena, L., 2020. New insights into seismic absorption imaging, *Phys. Earth planet. Inter.,* **298,** 106337.

Takahashi, T., Sato, H., Nishimura, T. & Obara, K., 2007. Strong inhomogeneity beneath Quaternary volcanoes revealed from the peak delay analysis ofS-wave seismograms of microearthquakes in northeastern Japan, *Geophys. J. Int.,* **168**(1), 90–99.

Takahashi, T., Sato, H., Nishimura, T. & Obara, K., 2009. Tomographic inversion of the peak delay times to reveal random velocity fluctuations in the lithosphere: method and application to northeastern Japan, *Geophys. J. Int.,* **178**(3), 1437–1455.

Tisato, N. & Quintal, B., 2014. Laboratory measurements of seismic attenuation in sandstone: strain versus fluid saturation effectsStrain and saturation effects, *Geophysics,* **79**(5), WB9–WB14.

Tobias, A., 1976. Acoustic-emission source location in two dimensions by an array of three sensors, *Non-Destr. Test.,* **9**(1), 9–12.

Tripathi, J. N., Sato, H. & Yamamoto, M., 2010. Envelope broadening characteristics of crustal earthquakes in northeastern Honshu, Japan, *Geophys. J. Int.,* **182**(2), 988–1000.

Unakafova, V. & Keller, K., 2013. Efficiently measuring complexity on the basis of real-world data, *Entropy,* **15**(10), 4392–4415.

Vlastos, S., Liu, E., Main, I. G. & Narteau, C., 2007. Numerical simulation of wave propagation in 2-D fractured media: scattering attenuation at different stages of the growth of a fracture population, *Geophys. J. Int.,* **171**(2), 865–880.

Waibel, A., Hanazawa, T., Hinton, G., Shikano, K. & Lang, K. J., 1995. Phoneme recognition using time-delay neural networks, in *Backpropagation: Theory, Architectures and Applications,* pp. 35–61, eds Chauvin, Y. & Rumelhart, D.E., Taylor & Francis.

Yoshimitsu, N., Furumura, T. & Maeda, T., 2016. Geometric effect on a laboratory-scale wavefield inferred from a three-dimensional numerical simulation, *J. appl. Geophys.,* **132,** 184–192.

Zhang, G., Li, H., Wang, M., Li, X., Wang, Z. & Deng, S., 2019. Crack-induced acoustic emission and anisotropy variation of brittle rocks containing natural fractures, *J. geophys. Eng.,* **16**(3), 599–610.